



저작자표시-비영리-변경금지 2.0 대한민국

이용자는 아래의 조건을 따르는 경우에 한하여 자유롭게

- 이 저작물을 복제, 배포, 전송, 전시, 공연 및 방송할 수 있습니다.

다음과 같은 조건을 따라야 합니다:



저작자표시. 귀하는 원저작자를 표시하여야 합니다.



비영리. 귀하는 이 저작물을 영리 목적으로 이용할 수 없습니다.



변경금지. 귀하는 이 저작물을 개작, 변형 또는 가공할 수 없습니다.

- 귀하는, 이 저작물의 재이용이나 배포의 경우, 이 저작물에 적용된 이용허락조건을 명확하게 나타내어야 합니다.
- 저작권자로부터 별도의 허가를 받으면 이러한 조건들은 적용되지 않습니다.

저작권법에 따른 이용자의 권리는 위의 내용에 의하여 영향을 받지 않습니다.

이것은 [이용허락규약\(Legal Code\)](#)을 이해하기 쉽게 요약한 것입니다.

[Disclaimer](#)

이학석사학위논문

Velocity structure of upper mantle
discontinuities from waveform
modelling of triplicated phases
using Korean station

한반도 관측소와 트리플리케이티드 파형 모델링을
이용한 상부 맨틀 불연속면의 속도 구조

February 2016

Graduate School of Earth and Environmental Sciences
Seoul National University
Seismology Major

Sungwon Cho

Abstract

The mantle transition zone and its discontinuities are keys to understanding the complex nature of mantle convection. Northwest Pacific region has many earthquakes and seismic stations, so it is one of the best locations to study the mantle transition zone. Triplicated phases travel through and carry the velocity information near the discontinuities. Waveform modelling of these phases can reveal detailed structure near the mantle transition zone. Korean seismic stations and two earthquakes from the Izu–Bonin–Mariana arc are used for the triplicated waveform modelling. Synthetic waveforms are calculated by Kennett reflectivity code. Grid search of models and calculating variance reductions are used to compare synthetics and observations is applied for each event. The best result for each event showed slow upper mantle and deep discontinuities. To make a better model that explains both events, models that match arrival times the best are found by trial and error. First, the arrival times of phases travel above the discontinuity are matched with the synthetic wave's arrivals. Then those travel through deeper regions are matched by trial and error. The best model has 2% slow upper mantle, 440km deep 410 discontinuity, and 3% fast layer below 530km depth. This is consistent to the mantle wedge and stagnant slab found beneath the northern Philippine Sea.

Keyword : Mantle transition zone, Northwestern Pacific, Northern Philippine Sea, triplication, stagnant slab, mantle wedge, waveform modelling

Student Number : 2013–20343

Table of Contents

Abstract	i
Table of Contents.....	iii
List of Tables	iv
List of Figures	v
Chapter 1. Introduction.....	1
Chapter 2. Backgrounds.....	5
2.1. Mantle transition zone	5
2.2. Previous studies in the northwest Pacific region.....	6
Chapter 3. Observation data	9
Chapter 4. Triplication waveform modelling	15
Chapter 5. Results.....	24
Chapter 6. Discussion.....	39
Chapter 7. Conclusion and further studies	41
References	43
Abstract in Korean.....	47

List of Tables

1. List of events used in this study.	10
--	----

List of Figures

1. (a) Reduced P wave travel time diagram for 100km depth event. Blue line indicates the distance for imaginary station at 25 degree. (b) Triplicated rays for imaginary station at 25 degree from the source. 2
2. Map of events (stars), stations (blue triangles) used for the waveform modelling and bottoming points for each event (cross). Black ones from NE1, Red ones from NE2, Green ones from SE1, blue ones from SE2. Black and red lines indicate the slab surface of the Pacific and Philippine Sea Plate with 100km depth intervals. Red dashed line indicates the line of cross section in Figure 4. 11
3. (a) The procedures to make reference waveforms (a) and deconvolution (b). The upper 6 waveforms in (a) are waveforms cut to make a reference waveform and the bottom one is the resultant reference waveform. The upside of (b) is the original waveform and downside is devonvoluted waveform. Deconvoluted one has less noise and clear peaks. 13
4. The cross section of the study area in figure 2. B indicates the subducting Philippine slab beneath Japan. C is fast, cold stagnant Pacific slab and D is slow mantle wedge 14
5. Comparison of three synthetic codes. Saikia's (blue), Kennett's (green) and Zhu's (red). 18
6. The result of sensitivity test (a to d). The models used for the test (e) and lenend (f). 20
7. Observation waveforms of SE1. Black dots indicate arrival times calculated from IASP91 model. Black lines are observations and thick parts of them are used to variance reduction calculation. Blue dotted lines indicate trend of peaks. 25

8. The example of failure of variance reduction calculation. All labels are the same with the Figure 7	26
9. One of the best fitting models for SE1. This one has the deepest 410 discontinuity. All labels are the same with the Figure 7.	27
10. One of the best fitting models for SE1. This one has medium 410 discontinuity. All labels are the same with the Figure 7.	28
11. One of the best fitting models for SE1. This one has the shallowest 410 discontinuity. All labels are the same with the Figure 7.	29
12. Observation waveforms of SE2. All labels are the same to the Figure 7. The blue arrow indicates the peak considered to be 660 phase. Waveform from ULLB station is marked with its name.	31
13. The best model for event SE2 after manual inspection. All labels are the same with the Figure 7	32
14. Combined plot of SE1 (black) and SE2 (red). First arrivals are indicated in green line and second arrivals are in blue line.	34
15. Best model for upper layer arrival time fitting. Black lines are observations and red ones are synthetics. The Second arrivals fit well, but the first arrivals do not fit in far stations.	36
16. Best model after fitting for one linear structure between 410 and 660. The first arrivals near 19° does not fit well. .	37
17. The best model. The phase between the 440 and 530 follows the green line and that below the 530 follows blue line	38

Chapter 1. Introduction

The mantle transition zone is the place where materials in the upper mantle transforms into those in the lower mantle. Its upper and lower boundaries are located on the 410km and 660km depth, called 410km and 660km discontinuities (referred to here as the 410 and 660). The minerals experience phase transition controlled by many factors such as temperature and chemical composition. These properties can be used to understand the thermal and chemical convection inside the mantle, so many geologists and geophysicists studied there to understand nature of the Earth.

Many methods are used to study the mantle transition zone and seismic waveform modelling is one of them. It makes synthetic waveforms, compares them with observation and finds the best structure which explains the observed data. Triplicated phases (Figure 1), which travel above, beneath, and reflected at a discontinuity, can be recorded in seismograms with close arrival times in regional distances. They have the information near the discontinuities, so we can use waveform modelling of triplicated phases to study the mantle transition zone.

The northwest Pacific is the place where the Pacific, Philippine, and Eurasian plates meet each other and sink down into the mantle. This region is one of the best places to study the interior of the Earth because there are many earthquakes, volcanoes, and seismic stations such as F-net in Japan or NECESS array in China

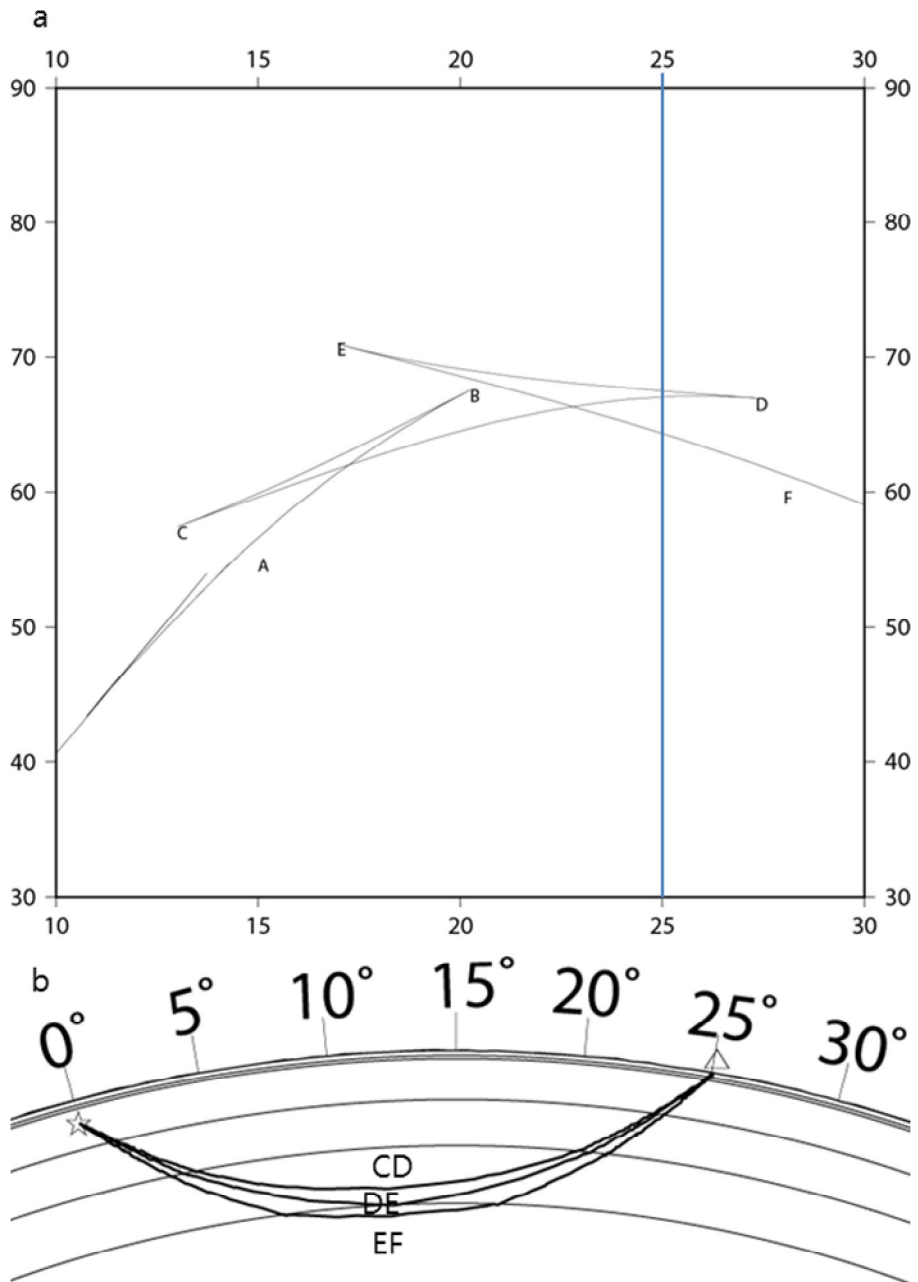


Figure 1 (a) Reduced P wave travel time diagram for 100km depth event. Blue line indicates the distance for imaginary station at 25 degree. (b) Triplicated rays for imaginary station at 25 degree from the source.

[Takeuchi et al., 2014]. It is known that the subducted Pacific slab is stagnated in the mantle transition zone beneath Korea, northeast China, and the Philippine Sea. Stagnant slabs were observable in both global and local tomography and waveform modelling studies. But in some regions, high velocity anomaly beneath the 660 is found, which seems like the stagnant slab finally breaks and falls to the lower mantle [Li and van der Hilst, 2010].

In this study, I will model triplicated waveform data from Korean stations to understand the mantle transition zone beneath the northwestern Pacific region. Many researchers studied this region to understand the structure of mantle transition zone and its discontinuities. However, they rarely used Korean seismic stations, especially those using the waveform modelling of triplicated phases. There are about 50 broadband seismic stations in Korea (Figure 2.) and most of them are not far from each other. Previous researches show that the triplicated waveforms can vary a lot even in small change of triplicated points. The close distribution of Korean seismic stations can help observing this characteristic of triplicated waveforms.

Also, the triplication points of Korean stations are far from previous studies with Chinese stations. The range which triplicated phases can be observed vary with the source and structure, but it is generally $15\sim 30^\circ$ from the epicenter. There are three subduction zones coincides this condition. Kuril Islands, Izu-Bonin-Mariana Trench, and Philippine Trench are them. Waves from Kuril Islands meet the discontinuities beneath the northeastern Eastern Sea,

West to the Sakhalin and Hokkaido while those from Izu–Bonin–Mariana Trench and Philippine Trench pass them under the northern Philippine Sea. Since there are subducting slab near the discontinuities in both regions, studying these regions can help us to understand the mantle discontinuities, subducting slabs, and their interactions. Triplicated waveforms recorded at Korean stations can provide additional information to supplement previous studies since they sample different places of 410 and 660 from those at Japanese or Chinese stations.

Chapter 2. Backgrounds

2.1. Mantle transition zone

Olivine is the most abundant material in upper mantle. At the 410km depth, it is transformed to wadsleyite and properties like density or seismic velocity are changed. This wadsleyite is transformed into spinel structure near 520km depth and then perovskite is formed at 660km. Each phase has different physical properties, so their boundaries, called discontinuities, can be observed by several methods.

The depths of discontinuities can be changed from various reasons. One of the most famous and traditional factor is the temperature. The phase transition at the 410 is exothermic, while it is endothermic at the 660. So in cold regions, the 410 becomes shallower and the 660 becomes deeper, which makes the mantle transition zone thicker. The opposite happens in hot regions, so the depth of the 410, 660, and the thickness of the mantle transition zone can be used as the indicator of the regional temperature.

Water transported by subducting oceanic slab can make changes near the mantle transition zone, too. Water solubility of wadsleyite in the transition zone is much higher than that of olivine, so more water makes the stable range of wadsleyite larger [Wood, 1995]. Therefore, the transition zone and the 410 become thicker where water content is high. Also, water can change the Clapeyron

slope and discontinuity depth will be changed, especially in lower temperatures [Litasov et al., 2006]. If there is enough water incorporated inside the mantle mineral, it is possible to make partial melting and low velocity layer by lowering the solidus [Inoue, 1994].

Chemical composition can also change the properties of mantle transition zone. For example, Mg content increase in $(\text{Mg,Fe})_2\text{SiO}_4$ makes the 410 deeper [Katsura and Ito, 1989]. Perovskites under the 660 is also made from garnet and this transition is exothermic, opposite from the spinel to perovskite transition [Yusa et al., 1993]. Subducted garnet-rich oceanic crust can exist to the transition zone and be shown as high velocity layer. The aluminum content has complex effect to the 660, which depends on the temperature [Weidner and Wang, 1998].

Subducting slabs and rising plumes can make the discontinuity change with the factors mentioned before. Also, earthquakes, seismometers, and appropriate geometry of them are required to study those regions. In NW Pacific, the Pacific plate is subducting beneath the Eurasian and Philippine plate and there are many seismic stations in Japan, Korea, and China. Therefore, it is one of the best places to study the mantle and many features of there are found.

2.2. Previous studies in the northwest Pacific region

The most famous mantle feature beneath the northwest Pacific

region will be the subducting Pacific slab. The Pacific slab is observed from mantle tomography studies like Huang and Zhao (2006) or Li and van der Hilst (2010). They observed stagnant slabs beneath Korea, northeast China, and Philippine Sea, which are formed by the subducting Pacific plate. The mantle transition zone in and near the Pacific slab is thicker [Gao et al., 2010] and the 660 depth beneath the Philippine Sea is deeper due to the stagnant slab [Suetsugu et al., 2010].

Many waveform modelling studies are also done in this region. Tajima and Grand (1998), Tajima et al. (2009), and Li et al. (2013) used waveform modelling of triplicated phases to study northeastern China. They suggested model with the depressed 660 to 690km and high velocity anomaly between 525 and 660km and model similar to previous one but without depression of the 660 can be used to explain the study area. In the study of Tajima et al., the structure change in this region cannot be explained by temperature gradient with the slab, so they suggested garnet-rich subducted oceanic crust acts like high velocity anomaly and flows to the nearby regions [Tajima et al., 2009].

Recently, Wang et al. (2014) observed the effect of subducting slab on seismic waveforms with 2D/3D synthetic waveform modelling. They used Chinese stations and earthquakes from Kuril Islands. Synthetic waveforms were made by reflectivity method and spectral element method. They showed the waveforms are sensitive to the structure and geometry of subduction zones and it is important to consider the shape of slab when applying 1D model to

subduction zones. They made 3D velocity structure model with a fast, 100km thick slab for close region; no velocity anomaly of slab under 560km for data near 20.5 degrees; and a low velocity zone above the discontinuity for farther data.

Chapter 3. Observation data

Triplication of P wave is recorded on seismographs between 15 to 30 degrees away from the source. I searched the earthquakes with same range from Korean stations occurred from 2006 to 2012. Seismograms from 3-component broadband seismographs of Korea Meteorological Administration and Korea institute of Geoscience and Mineral Resources were used in this study. I used earthquakes with magnitude between 5 and 7 to reduce the effect of source time function. Earthquakes with source depth shallower than 100km were excluded to avoid depth phases. 140 earthquakes were found from these criteria. I removed mean and linear trend from observed waveforms from Korean stations and applied band-pass filter with 0.04 and 1Hz corner frequency. 24 earthquakes with observable first P wave arrival were selected manually.

For these 24 earthquakes, seismograms of farther stations (30 to 60 degrees) with same azimuth range are obtained and same treatment was applied to produce reference waveform. Far-field P wave arrivals in this range can be assumed as source-time function because no other phase arrives near them. Only 4 earthquakes (Table 1 and Figure 2) showed observable and consistent P wave arrivals. Two earthquakes of the final 4 earthquakes are located in the Kuril subduction zone and the other two are located along the Izu-Binin-Mariana arc. I manually picked the peak of P wave

Table 1 List of events used in this study.

ID	Date	Latitude	Longitude	Depth	Mag
NE1	2007/03/30 09:05	44.131	146.070	102.6	5.5
NE2	2012/03/12 12:32	45.239	147.609	110.4	5.5
SE1	2009/07/29 14:52	22.657	143.307	136.5	5.5
SE2	2011/02/22 14:09	22.193	143.849	111.8	5.5

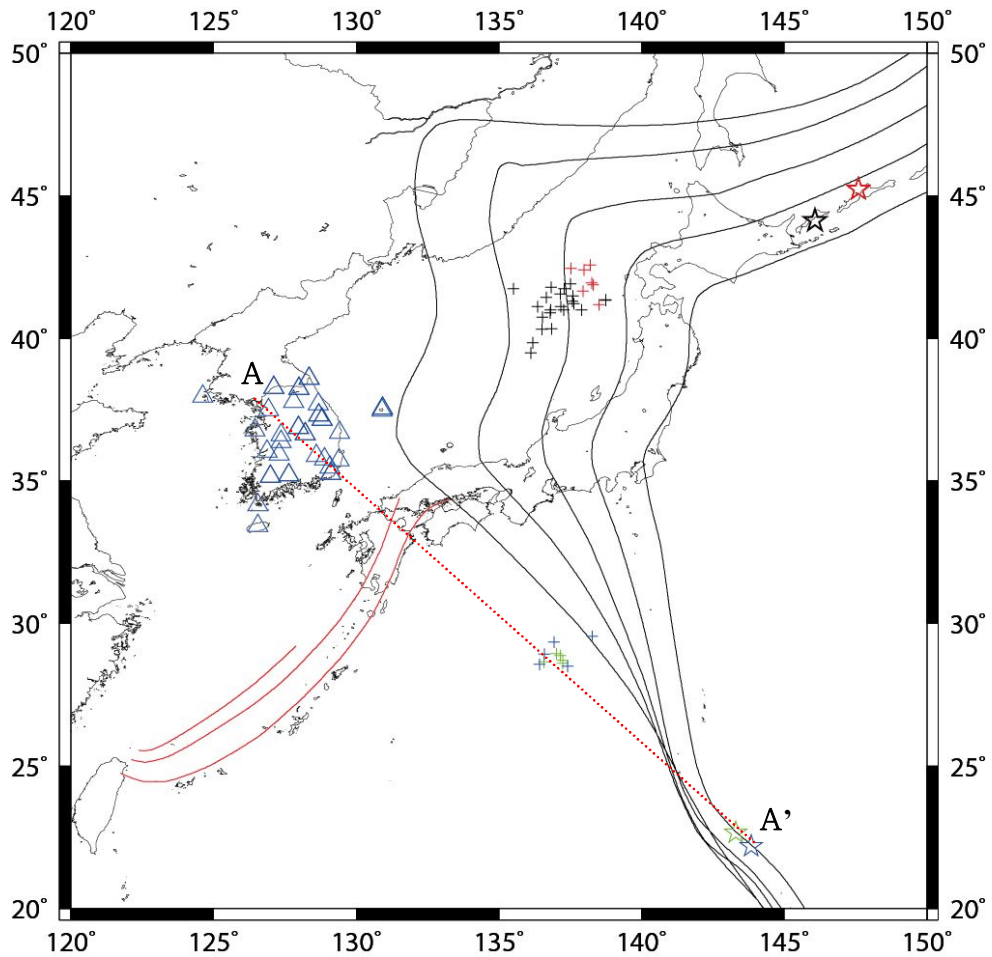


Figure 2 Map of events (stars), stations (blue triangles) used for the waveform modelling and bottoming points for each event (cross). Black ones from NE1, Red ones from NE2, Green ones from SE1, blue ones from SE2. Black and red lines indicate the slab surface of the Pacific and Philippine Sea Plate with 100km depth intervals. Red dashed line indicates the line of cross section in Figure 4.

arrivals of farther stations and cut 5 seconds before and after the arrival, leaving 10 seconds waveform. For each event, I normalized, summed, and then normalized these waveforms and set the result as the reference source time function (Figure 3.).

Four earthquakes I used are marked as NE1, NE2, SE1, SE2 in order of the event date and location. Northeastern events have theoretical bottoming points near 40°N and 138°E and the surface of the Pacific slab is about 300km there. On the other hand, the southeastern events have bottoming points around 28°N and 137°E where the Pacific slab is deeper than 500km (Figure 2, Figure 4.). The southeastern events have close bottom points and less effect of slabs, so they are preferable for waveform modelling. So in this study, I concentrate on those southeastern events.

The triplicated phases with small amplitude and close arrival time difference can be shaded by the first arrivals if the source time function is long. Therefore I removed the source time function by deconvolution. I used Ammon's receiver function code [Ligorria and Ammon, 1999] to deconvolute reference waveforms from data. Low-pass Gaussian filter is applied and resultant pulse width is approximately 1 second, so isosceles triangular source-time function with 1 second length is applied to synthetic waveforms. After deconvolution, the observations are compared to the arrival times of IASP91 model and real arrival times are manually picked.

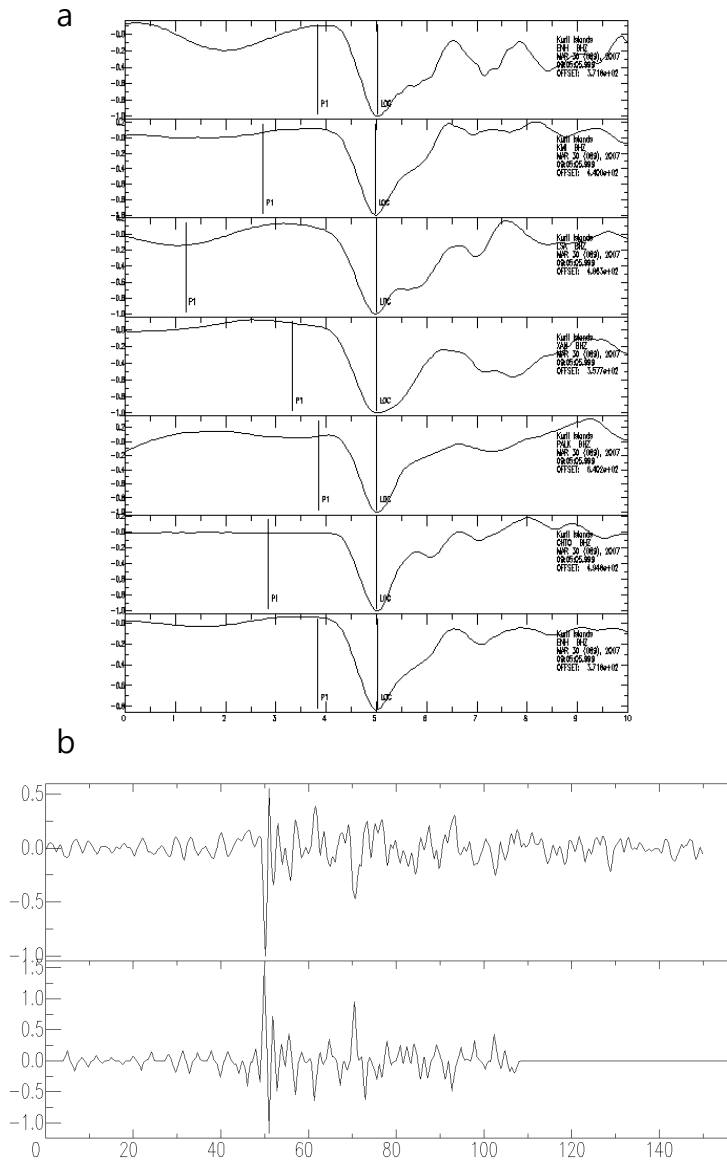


Figure 3 The procedures to make reference waveforms (a) and deconvolution (b). The upper 6 waveforms in (a) are waveforms cut to make a reference waveform and the bottom one is the resultant reference waveform. The upside of (b) is the original waveform and downside is devonvolved waveform. Deconvoluted one has less noise and clear peaks.

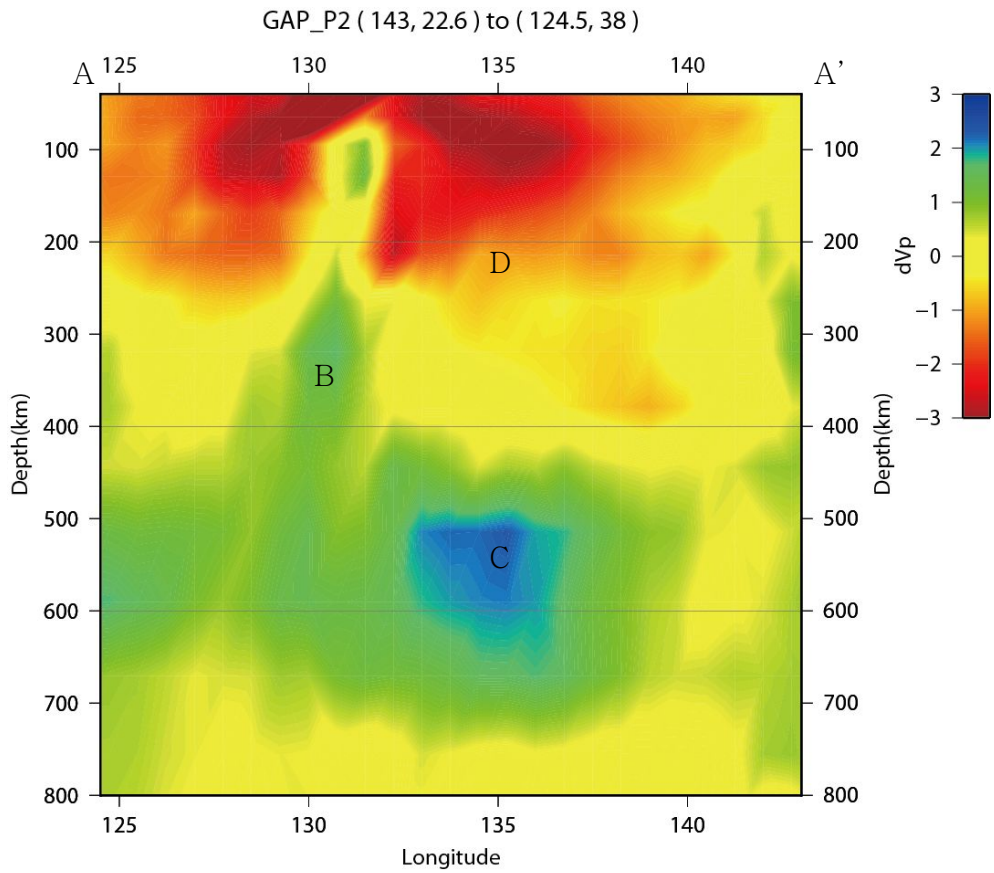


Figure 4 The cross section of the study area in figure 2. B indicates the subducting Philippine slab beneath Japan. C is fast, cold stagnant Pacific slab and D is slow mantle wedge.

Chapter 4. Triplication waveform modelling

Synthetic waveforms are calculated by the Reflectivity code of Kennett [Kennett, 1983]. It calculates seismic waveform of a point source with arbitrary moment tensor travel through uniform layers by reflectivity method introduced by Fuchs & Muller(1971).

Reflectivity method is a technique that calculates all reflections and conversions of waves in the structure. Let's say a stress-displacement jump vector Σ occurred across the source plane z_s . Σ can be represented with upgoing Σ_U and downgoing Σ_D . If we consider the upgoing part only, the surface response of this event will be the sum of direct transmission and multiple reflections of Σ_U . Σ_D will experience the same transmission and reflections after reflected from the underlying layer. This can be expressed as below.

$$w_0 = \tilde{W} [I - R_D^{OL} \tilde{R}]^{-1} T_U^{OS} [I - R_D^{SL} R_U^{OS}]^{-1} [\Sigma_U(z_s) + R_D^{SL} \Sigma_D(z_s)]$$

T_U^{OS} is the upward transmission matrix between the source and free surface(receiver level). R are reflection matrices in which R_D^{OL} is reflection matrix below the surface level(0) of downgoing(D) wave and R_U^{OS} is reflection matrix between surface level(0) and source level(S) upgoing(U) wave. \tilde{W} and \tilde{R} are displacement matrix and surface reflection matrix. In Kennett's code, separation level is introduced to make it easier to focus on shallow, slow

region or deeper wave propagation. Source effect is moved from the real source level to separation level and equivalent source is used for calculation. The reflection and transmission matrices of upper and lower part of separation level can be presented by those of layers inside each part. This \mathbf{w}_0 is in the slowness–frequency domain and to obtain theoretical seismograms, we need to integrate it over slowness and frequency. Integration is like the follow where $\mathbf{T}_m(\omega p r)$ is tensor field.

$$\bar{\mathbf{u}}(r, \mathbf{0}, \omega) = \frac{1}{2} \omega |\omega| M(\omega) \int_{-\infty}^{\infty} dp p [\mathbf{w}_0]^T \mathbf{T}_m(\omega p r)$$

In reflectivity method, this integration is done over a band of frequency and then over a slowness band.

To test synthetic waveforms from Kennett reflectivity code, I compared them with synthetic waveforms calculated from two FK codes, Saikia's [Saikia, 1994] and Zhu's [Zhu and Rivera, 2002]. For Zhu's code, we can input trapezoidal source time function and earthquake magnitude. However, Kennett reflectivity code does not have input for the magnitude while Saikia's resultant synthetics requires convolution with source time function. It is not simple to exactly verify these codes and correct these variables to the amplitude, so I just normalized waveforms and compared them.

The structure model for this test is a single uniform layer with $V_p=6\text{km/s}$, $V_s=3.5\text{km/s}$, $\rho=2.7\text{g/cm}^3$, $Q_s=5000000$, $Q_p=10000000$. Separation level for the Kennett reflectivity code is 40km. On Saikia's code, it is impossible to calculate with single layer, so I put the same layer below one. Event source depth is set to 100km and

station is located on 500km distance and 90 degrees azimuth. The moment tensor of the event is set to be explosive ((Mxx, Mxy, Mxz, Myy, Myz, Mzz)=(1, 0, 0, 1, 0, 1)) for simplicity of calculation and exponent is 21, practically found to have similar amplitude size with Kennett reflectivity code and Zhu's code. Isosceles triangular source time function with 1 second length is applied to Kennett reflectivity code and Zhu's code. For Saikia's code, source time function is convoluted after synthetic waveform is calculated.

The resultant waveforms (Figure 5) after normalization show same arrival time of P wave. Even though the waveforms have little difference at the beginning and ending of the pulse, the width and general shape of waveforms are the same and thus we can say that Kennett reflectivity code is reliable.

Triplicated waveform modelling assumes the waveform of triplicated phases is only sensitive to the mantle discontinuities' structures. Shallower parts like crust or upper mantle only affect the arrival time of first arrival, while the time differences and amplitude ratios between each phases are not affected. To verify this, I compared several models with different velocity structures.

The velocity structure models for this test are modified from the IASP91 earth model. For each layer above the 610km, I increased or decreased P wave velocity by 1, 3, 5, and 10 %. The structures of models beyond the 610km are same as the IASP91 model. Source is located on the free surface to make the ray path symmetric. The distance from the source to receiver is 2250km because it made the triplicated phases pass near the 410

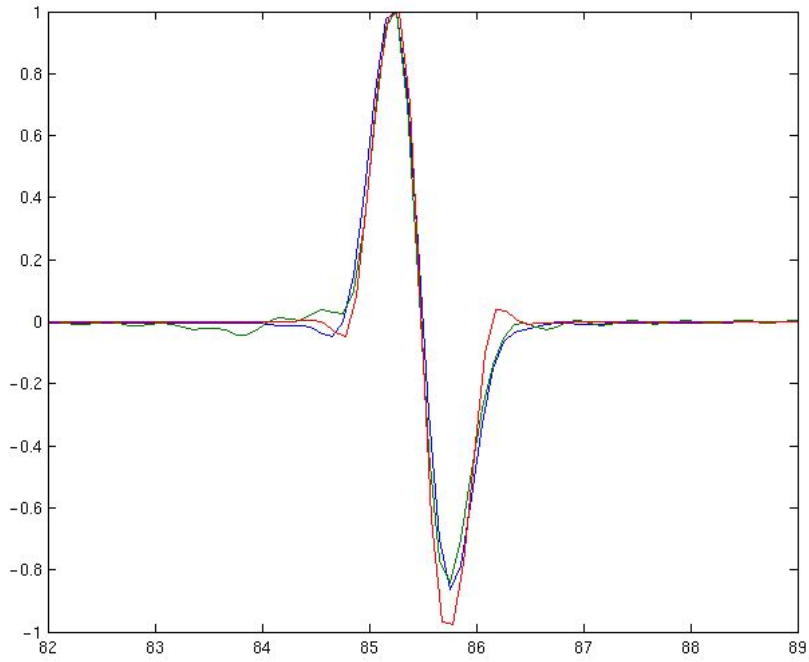


Figure 5 Comparison of three synthetic codes. Saikia's (blue), Kennett's (green) and Zhu's (red).

discontinuity and 660 phases away from 410 phases. Synthetic waveforms were made by the Kennett reflectivity code and best variance reductions and time shifts are calculated with the process described above. The triplicated phases arrive in order of refracted beneath 410, refracted above 410, and reflected at 410 in IASP91 model.

The time shifts and variance reductions from each model are on the figure. The crustal structures seem to have very little effect on waveform since the minimum variance reduction of crustal structure, obtained from the model with 10% faster crust, is still higher than 95. However, the velocity changes in crust can delay or haste the P wave arrivals more than 1 second.

For most models, velocity changes shallower than 210km have variance reductions more than 80 except the 10% faster variations (Figure6.). 10% fast layer models show variance reduction drop with fast layer deeper than the crust and this may be caused by significant change of ray path. However, most tomography results show the mantle velocity perturbation less than 5% [Fukao et al., 2009], so I can exclude these models with extremely fast or slow models. Every model showed generally increasing time shift and decreasing variance reduction when depth and thickness of the anomaly layer increases. However, they are reduced when the anomaly layer becomes deeper. For models with anomaly layers beneath 460km depth, the ray refracted beneath 410km pass above the 460km depth, so the effect of anomaly layers is decreased. In the case of models with a fast layer in between 410km and 460km,

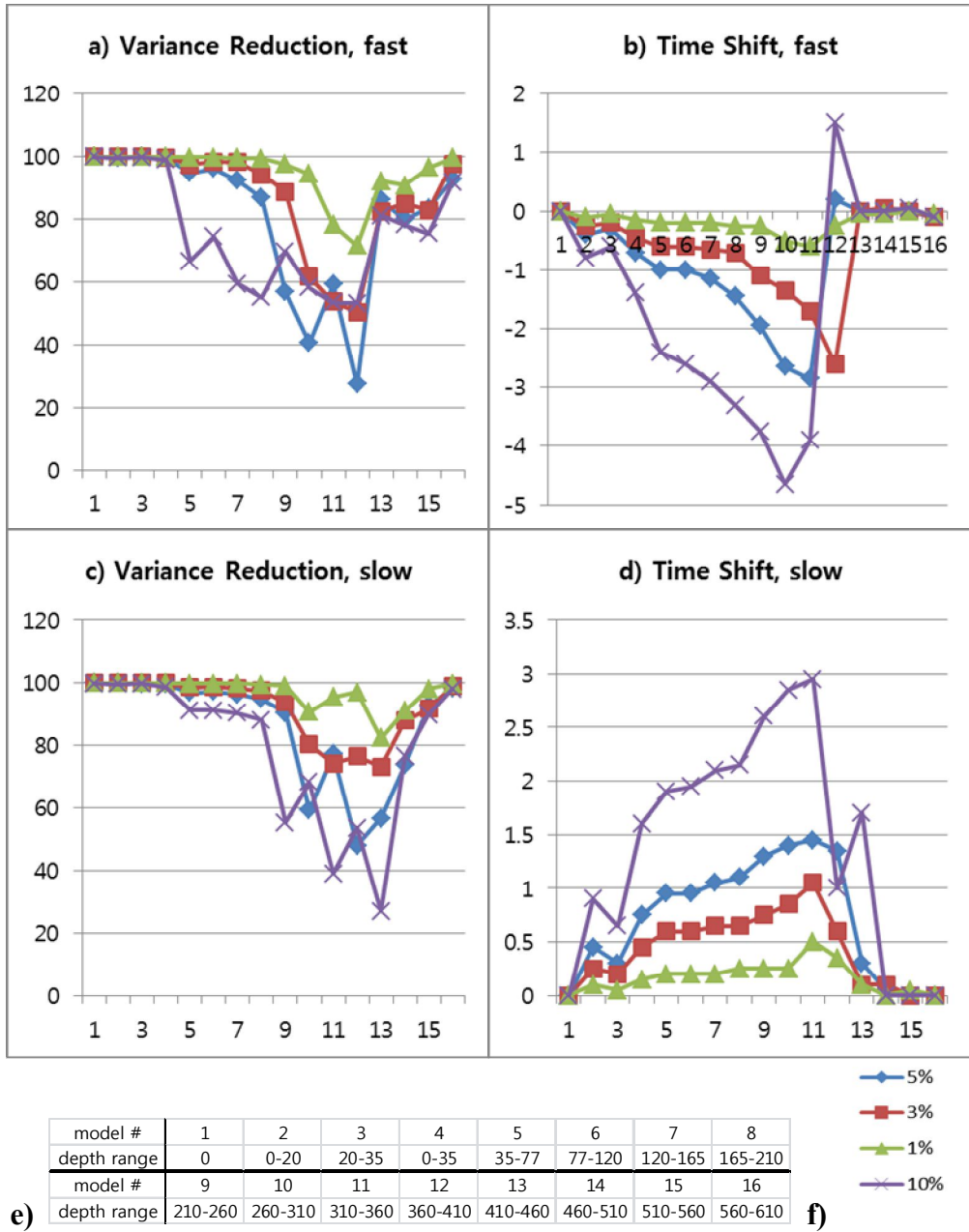


Figure 6 The result of sensitivity test (a to d). The models used for the test (e) and legend (f).

the amplitude of ray pass this layer is small, so the variance reductions are smaller than those with shallower fast layer. The model with a fast layer just above the 410km depth has minimum variance reduction but positive time shift while models with shallower fast layer has negative time shift. This may due to the fast velocity layer operates like uplifting of the discontinuity, so the waveforms are distorted and later, large amplitude phases are matched during the calculation.

Unlike the models with anomaly layers between 210km and 410km, those with anomaly layers shallower than 210km have generally high variance reductions. Only the model with 5% fast velocity layer in 165km to 210km has variance reduction of 86.7 and the others have variance reductions over 90. Compared to the models with anomaly layers near the 410 discontinuity, I can say that this waveform modelling is sensitive to the velocity structures near the discontinuity.

I used grid search to find the best discontinuity models for each earthquake. I changed 7 model variables of IASP91 model to make models the synthetic waveform calculation. Model parameters in between of 210, 410, and 660km boundaries are linearly interpolated with 10km interval. The velocity and density jump at the 660 discontinuity are removed to exclude their effect on synthetics and concentrate on 410 discontinuity. The parameters at the 660 km depth are those of IASP91 model's values just above the discontinuity. Below the 660km to 1000 km, each values were extrapolated from the values of the 660km and underside of 410

discontinuity. Velocity models with slower underside of discontinuity are considered unrealistic and excluded. About 2000 models are made with this process. Synthetic waveforms for each event and station are calculated by these models. Same band-pass filtering is applied to the waveforms.

To compare the synthetic and observed waveforms, I calculated variance reduction of waveforms. For observation, cosine tapers are applied near the first P wave arrivals to remove 660 phases and other late noises. The length of taper for each event is different from each other to include arrivals of 410 triplicated phases. Synthetic waveforms are cut from 4 seconds earlier to the start of taper to 4 seconds later to the end of taper. Variance reduction is calculated for same length, so for each observation and synthetic waveform pair, variance reductions are obtained for each time step from -4 seconds to +4 seconds. The best variance reduction for this pair and its time shift is selected as that of a station. Then I calculated average of variance reductions of stations in a model and set it as the model's variance reduction. The model with the maximum variance reduction should be the correct model for the event and explain the structure of the point where triplication occurs.

I tested this variance reduction calculation with synthetic waveforms to figure out that result finds the correct model. One model is selected as observation and I searched the best model with the same method. With waveforms without tapering, the test found the correct models used for the observations. When I applied

tapering, sometimes the best model found from the variance reduction is not the model of the observation. In this case, the tapering cut some later P wave arrivals and the correct models were found after adjusting tapering.

This method just compares each waveform and disregards difference of the first arrival time, so the result may show different trend of arrival times from the observation. Also, the tapering length can cause problems when comparing observations to the synthetics. Therefore, I manually checked waveforms with variance reductions larger than 90% of that of the best model and selected the final model which fits each waveform and trend of arrivals.

Chapter 5. Results

The SE1 event had 10 stations with clear P wave arrivals (Figure 7). But only half of them are used because others are far and have the possibility of contamination from 660 phases. Waveforms show clear two peaks (Figure 7 a and b) and a valley (Figure 7 c) which arrives after them. The peaks are close in shorter ranges, but they are separated about 4 seconds in the farthest station. The amplitude of the second peak also changes from small to large according to the distance. In this range and source depth, the first arrival might be the phase that bottom beneath the 410km depth and the second will be the one travel above the discontinuity.

In several models, the variance reduction often matched the peaks from observations with later peaks of synthetics (Figure 8.). These synthetics had high amplitude arrivals earlier than the phase matched to the first arrivals of observations. These clearly incorrect, high variance reduction models are removed manually.

Three models had high enough variance reduction and matching waveforms (Figure 9. to 11). None of them have slab or the fast 210 boundary. But all of them have different 410 discontinuity depth. The deepest one (Figure 9) has the 410 discontinuity at 430km, slower upside and faster downside at the discontinuity. The middle one (Figure 10) is similar to the IASP91 model except the

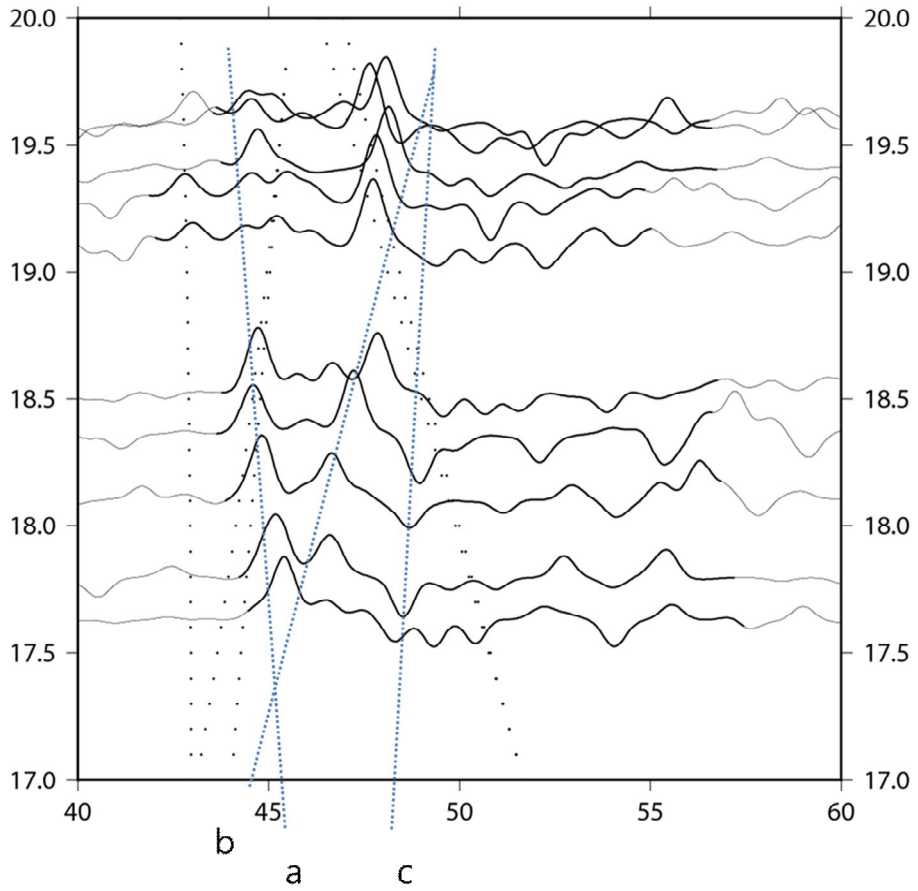


Figure 7 Observation waveforms of SE1. Black dots indicate arrival times calculated from IASP91 model. Black lines are observations and thick parts of them are used to variance reduction calculation. Blue dotted lines indicate trend of peaks

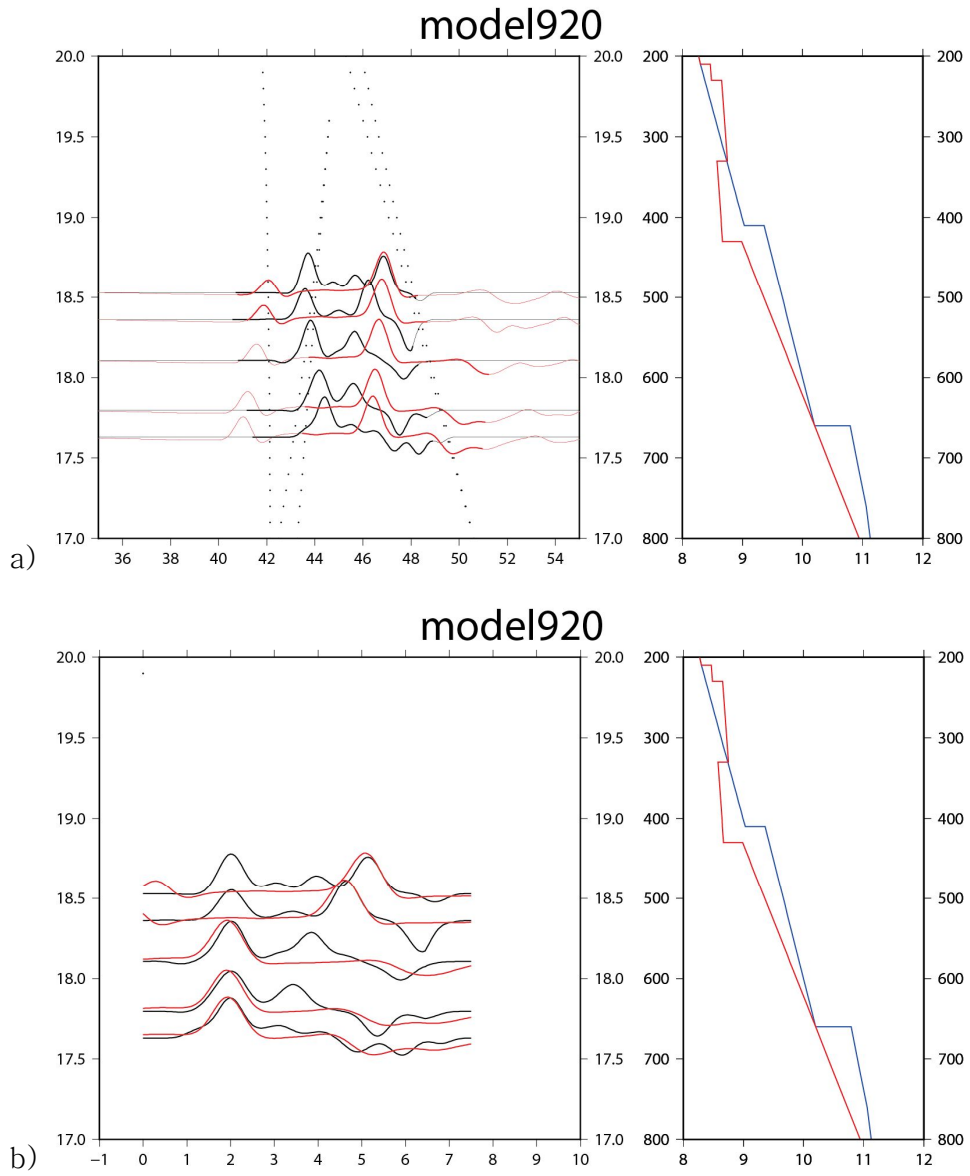


Figure 8 The example of failure of variance reduction calculation. All labels are the same with the Figure 7.

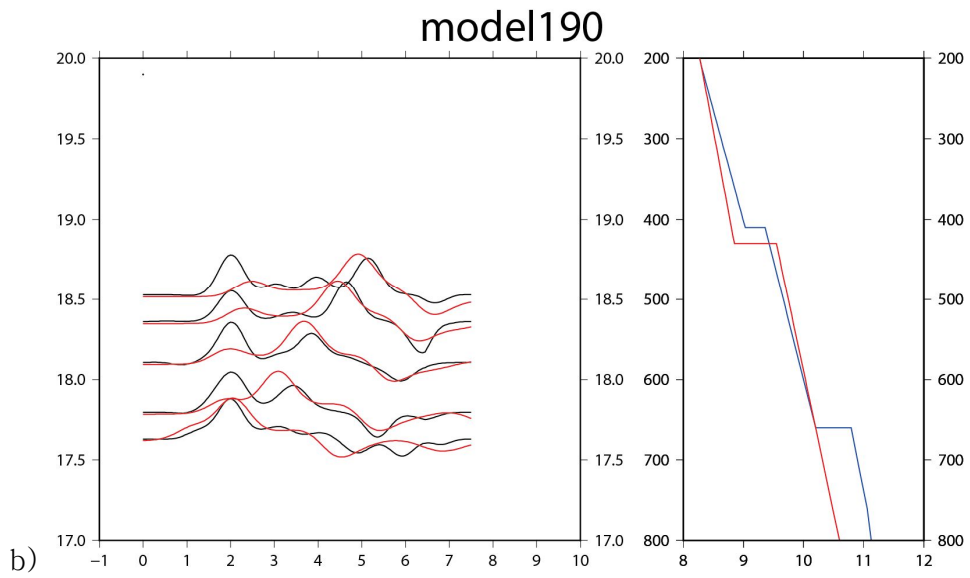
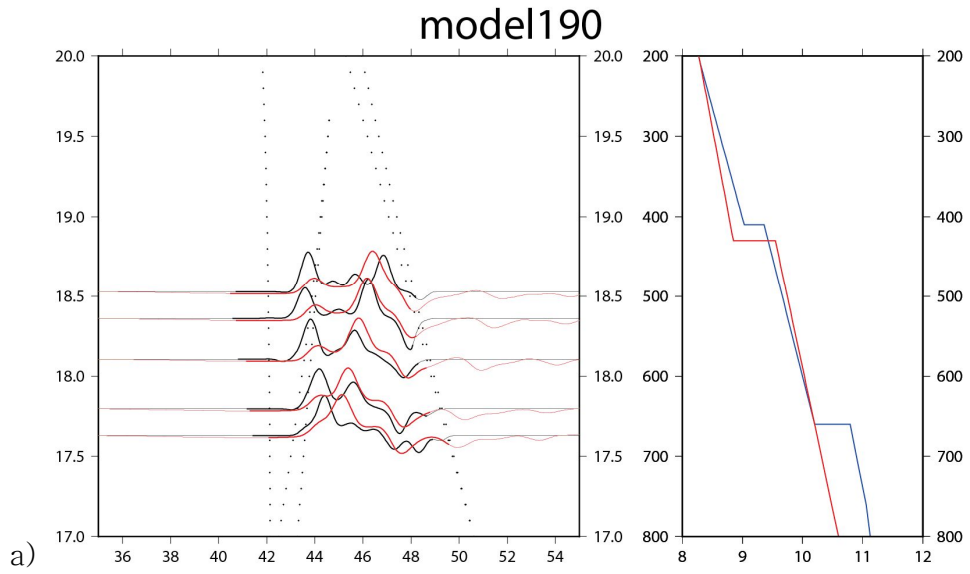


Figure 94 One of the best fitting models for SE1. This one has the deepest 410 discontinuity. All labels are the same with the Figure 7.

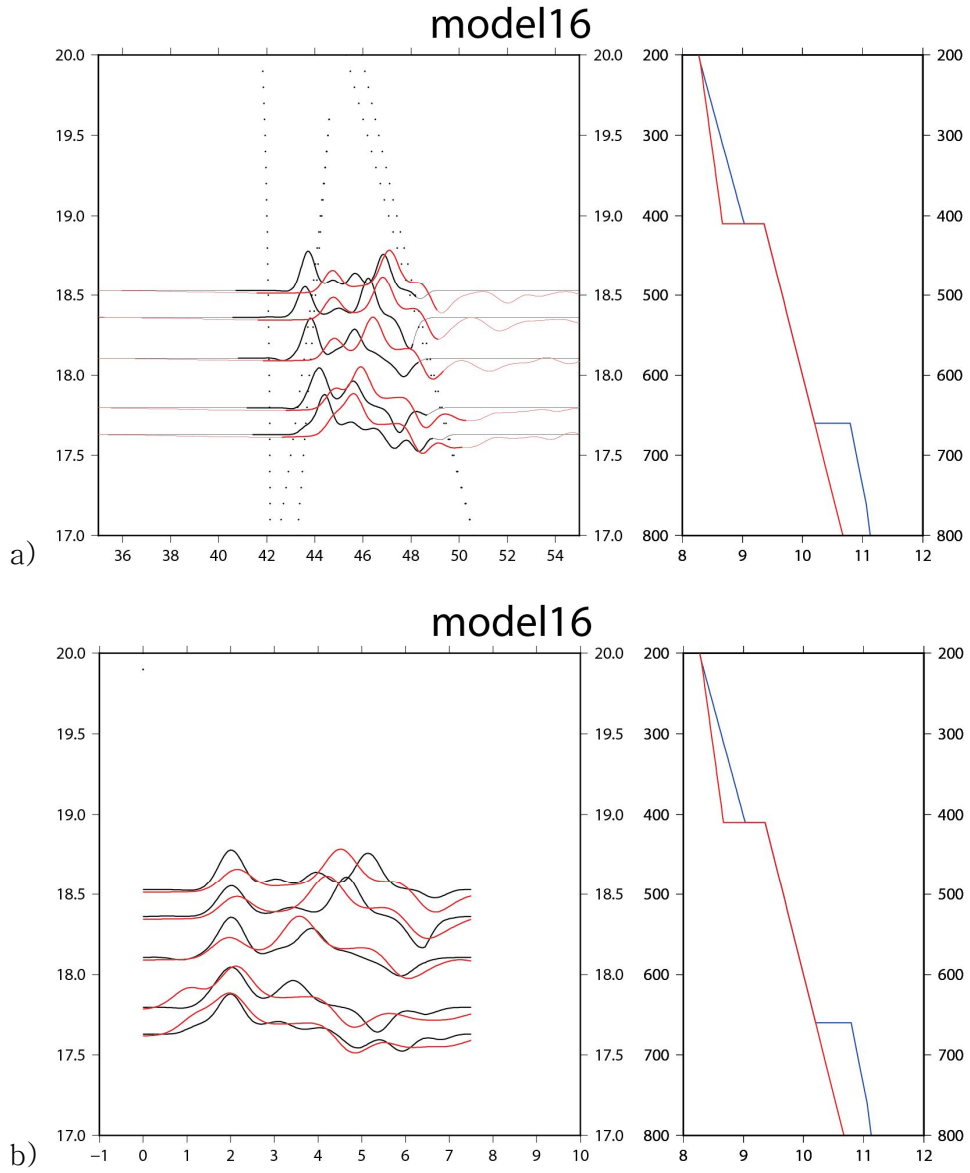


Figure 10 One of the best fitting models for SE1. This one has medium 410 discontinuity. All labels are the same with the Figure 7.

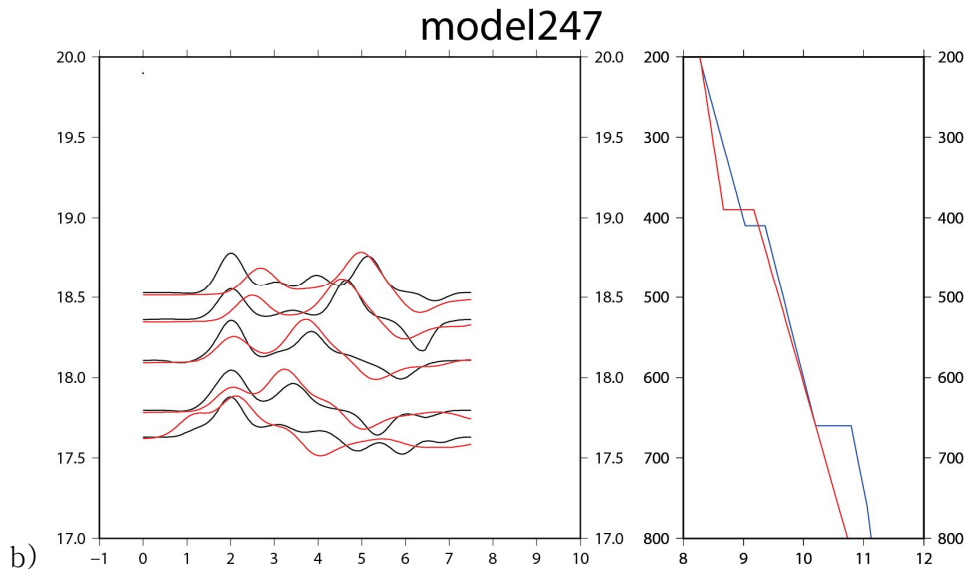
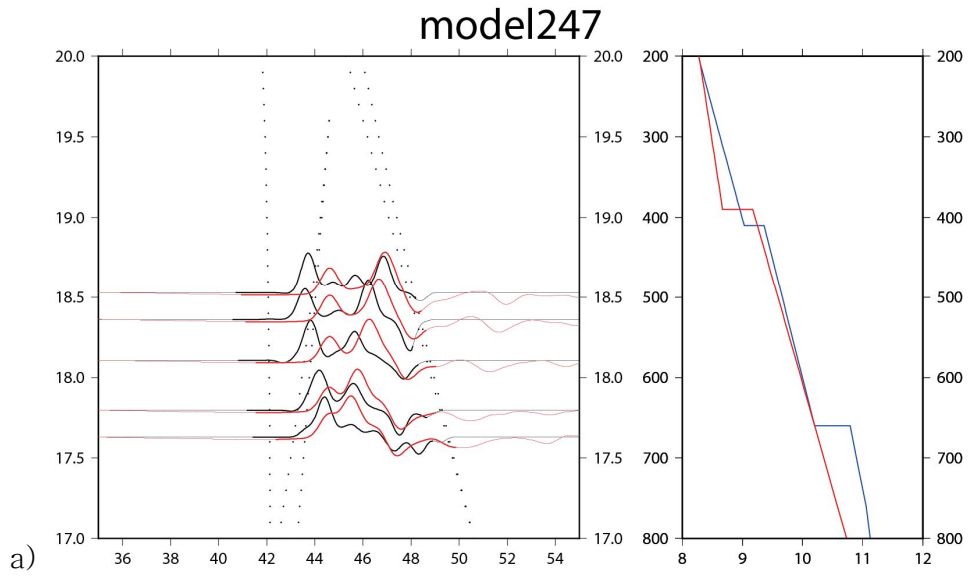


Figure 11 One of the best fitting models for SE1. This one has the shallowest 410 discontinuity. All labels are the same with the Figure 7.

velocity upside the discontinuity is low. The shallowest one (Figure 11) has the discontinuity at 390km and generally slow above and below the discontinuity. All these models show the widening pattern of the peaks but the deepest one matches the trend of peaks better than others. However, the deepest one has the smallest first arrival amplitude while the shallowest one has the largest. Since the shallower ones fit worse to the trend, the deepest one is the best fitting model. But their amplitude ratio suggests the model between the deepest and middle one, which is in the gap of the grid search, could make better synthetics.

The last event, SE2 is located farther than SE1, but its bottoming points are close to them of SE1. The trend is similar to SE1; the first, fast arrivals and the second, slow arrivals (Figure 12). SE2 also has the similar problems in SE1. Closest 5 stations are used in waveform modelling with short section for calculating variance reduction to prevent contamination. Even though to these efforts, the stations near the 20° shows peaks between the first and the last in the aligned view, which are considered to be the 660 phase (Figure 12, blue arrow). Matching of the first of observation to later ones of synthetic also occurred here. Also, the peaks from ULLB station arrives earlier compared to the trend from other events, so the manual inspection is more required.

Like to the SE1, SE2 had similar models differing the discontinuity depth and speed showed best waveforms. The best model (Figure 13) is the one with the discontinuity at the 430km depth and slow upside, fast downside of it. This model meets the

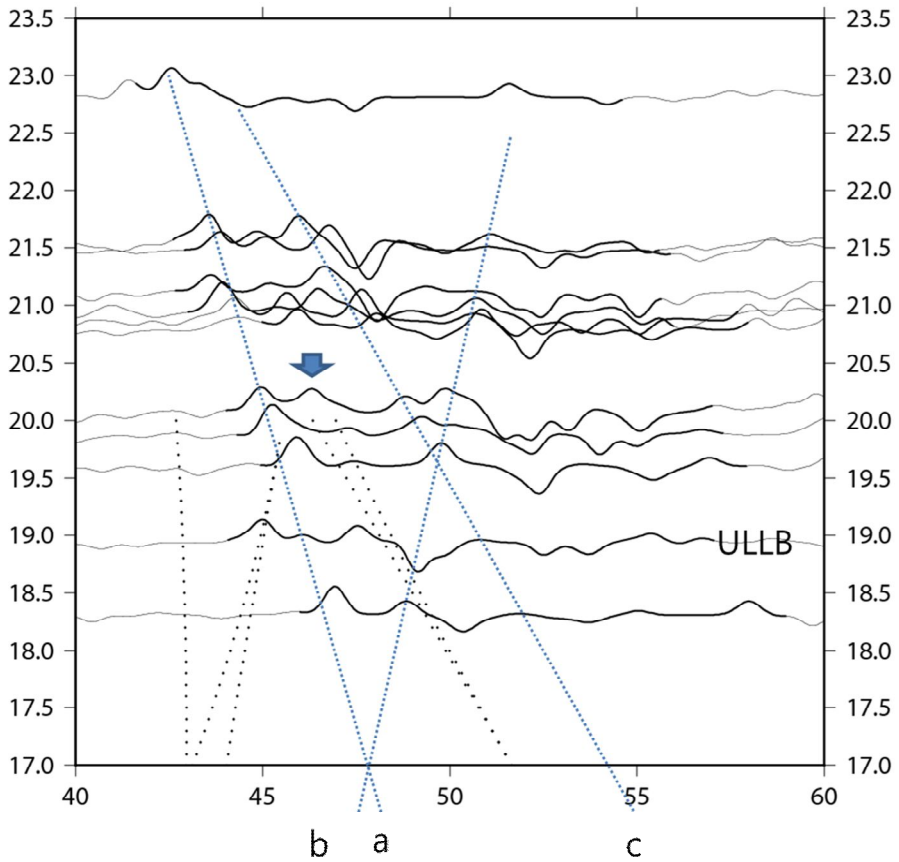


Figure 12 Observation waveforms of SE2. All labels are the same to the Figure 7. The blue arrow indicates the peak considered to be 660 phase. Waveform from ULLB station is marked with its name.

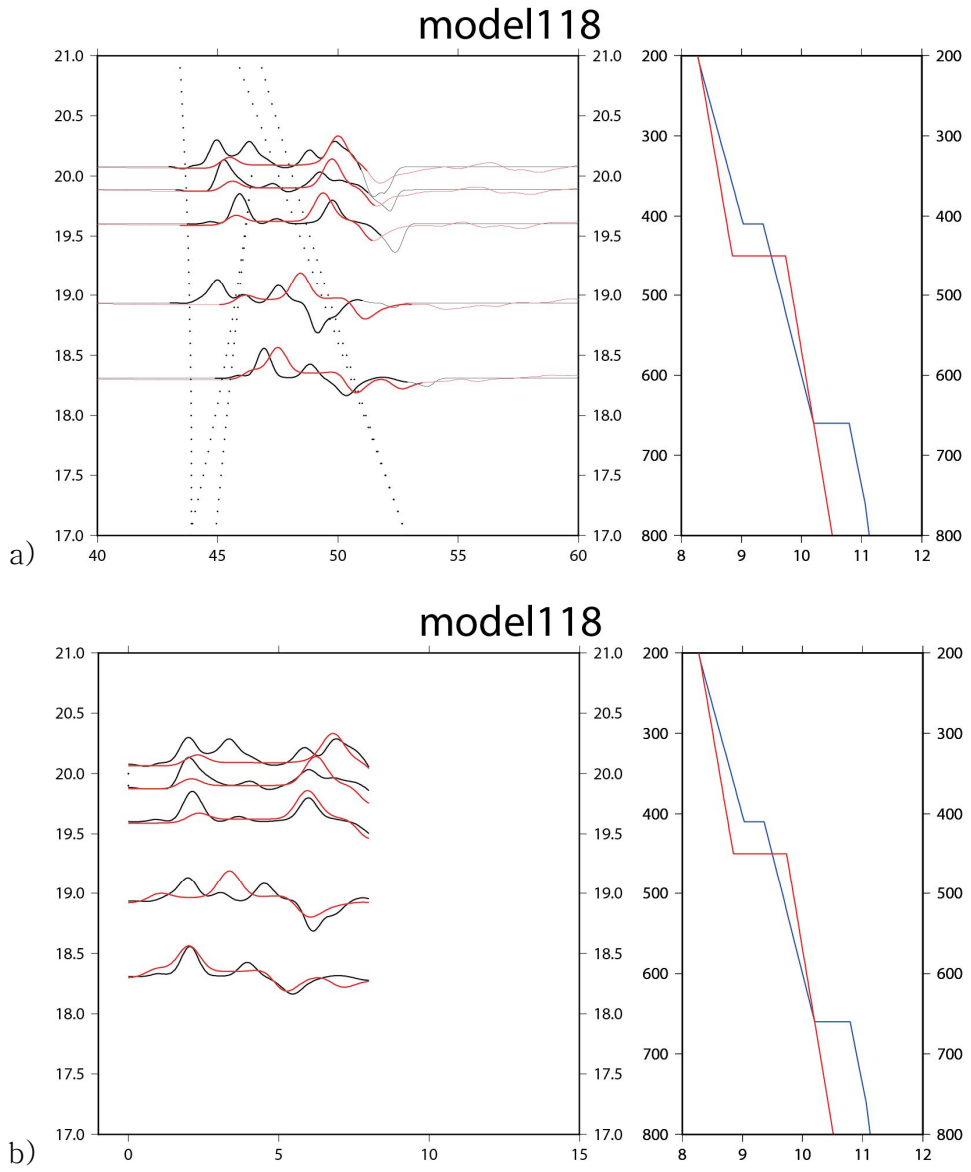


Figure 13 The best model for event SE2 after manual inspection. All labels are the same with the Figure 7.

arrival times of each peak closely while the amplitudes of the first arrivals are still small, similar to ones from SE1. It may seem to fail to match the ULLB waveforms in aligned plot, but small shifting would make the peaks to match correctly. The shallower ones have larger first arrivals, but their trends of first arrivals are different from the observations.

SE1 and SE2 have close bottoming points and similar patterns, but grid search method with variance reduction for each event failed to make one unifying model. I made synthetic waveforms to fit both events and explain the region in one model. In this time, the trend of arrival times are matched first without time shift and best model was made by trial and error.

To match the trend of arrival times, I first plotted waveforms of both events on same plot. The two events have different source depths, so arrival time correction is applied to SE1 event. The first arrival times for each stations in SE1 is calculated and is subtracted from those for same distances but source depth of SE2. The arrival time differences varied from 1.78s to 1.81s for closest to farthest stations. ULLB station's arrivals are faster than others because of the thin crust beneath it, so its arrivals are delayed 2s. The whole waveforms with arrival time correction are plotted in Figure 14.

The first arrivals (green line) are those travel beneath the 410 discontinuity and the second phases (blue line) are those travel above it. The second phases are slow and weak in farther stations. The first phase changes its velocity about 19 degrees and separated into two phases in farther regions, which means it could

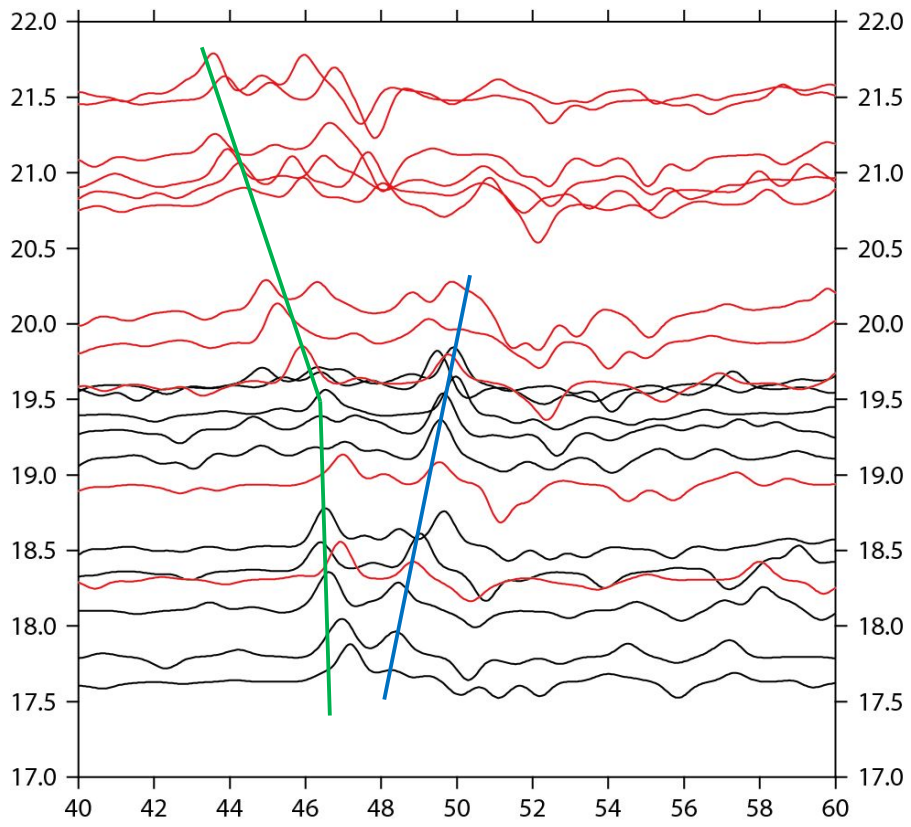


Figure 14 Combined plot of SE1 (black) and SE2 (red). First arrivals are indicated in green line and second arrivals are in blue line

be composed of two phases across another, unknown discontinuity.

Since the second phases travel the upper layers, so they are fitted first. To do this, the arrival times of phases travel above the discontinuities from different models are calculated. In these models, the velocity between the 35km and 410 discontinuities and the depth of it are changed. In detail, the 410 discontinuity depth and the velocity above it is changed and the velocity between 35km (just beneath the Moho) and 210km are multiplied by modifier. Then the structure between 210km and 410 discontinuity is interpolated. The best model has deeper 410 discontinuity and 2% slow velocity above it (Figure 15).

Then the first arrivals are matched by changing the structure beneath the 410 discontinuity. In here, the velocity beneath 410 discontinuity and the velocity and depth of 660 discontinuity are changed. Many models with linear structure between 410 and 660 are tested but the best model of them failed to fit the change of slope around the 19° range (Figure 16). To explain the trend change and separation at far distances, another layer with is introduced in this region. The best fitting model is on Figure 17. Its first arrivals in close ranges (17.5° to 18.5°) seems apart from the observation, but they are larger, second arriving phases shading small, earlier arrivals. The final model has 2% slow upper mantle, 410 discontinuity at 440km, the velocity above and below the 410 is 1% and 3% fast. The velocity comes close to the iasp91 value in the upper layer but it jumps to 103% after 530km.

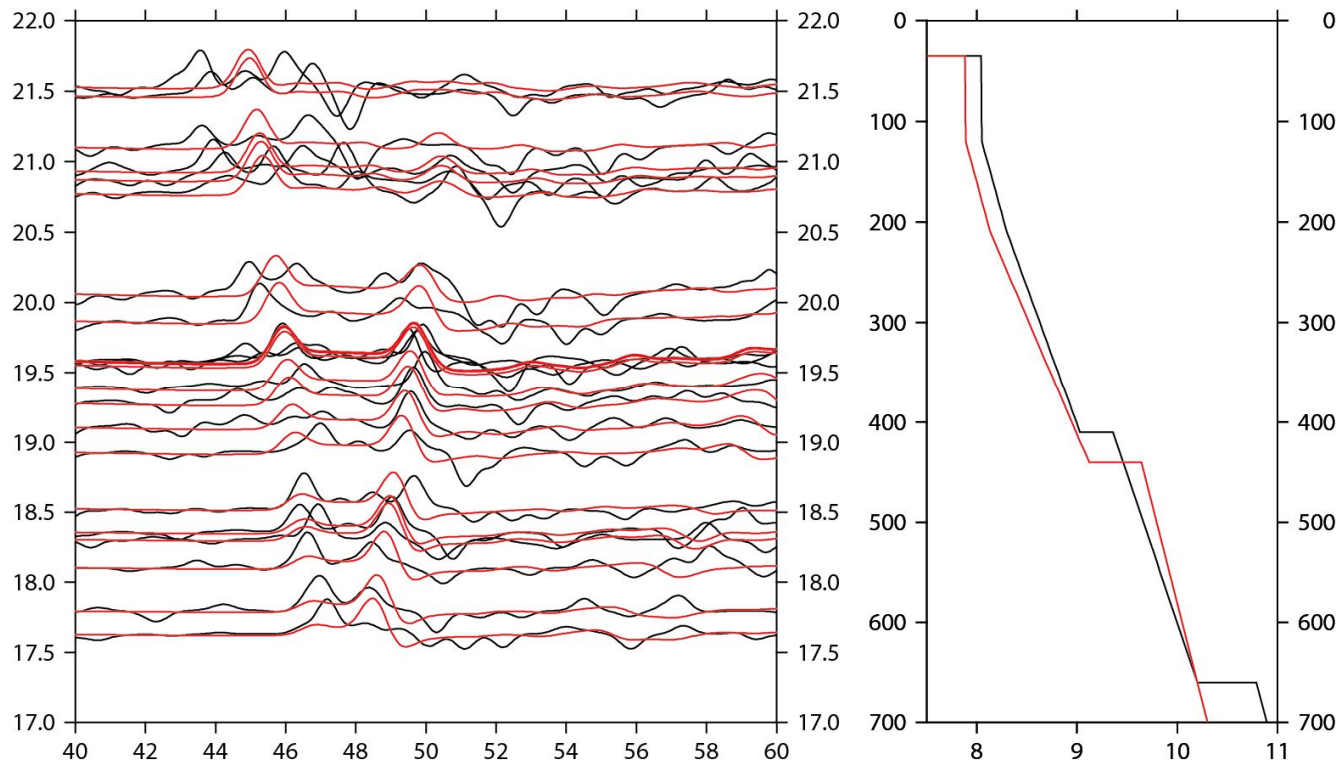


Figure 15 Best model for upper layer arrival time fitting. Black lines are observations and red ones are synthetics. The Second arrivals fit well, but the first arrivals do not fit in far stations.

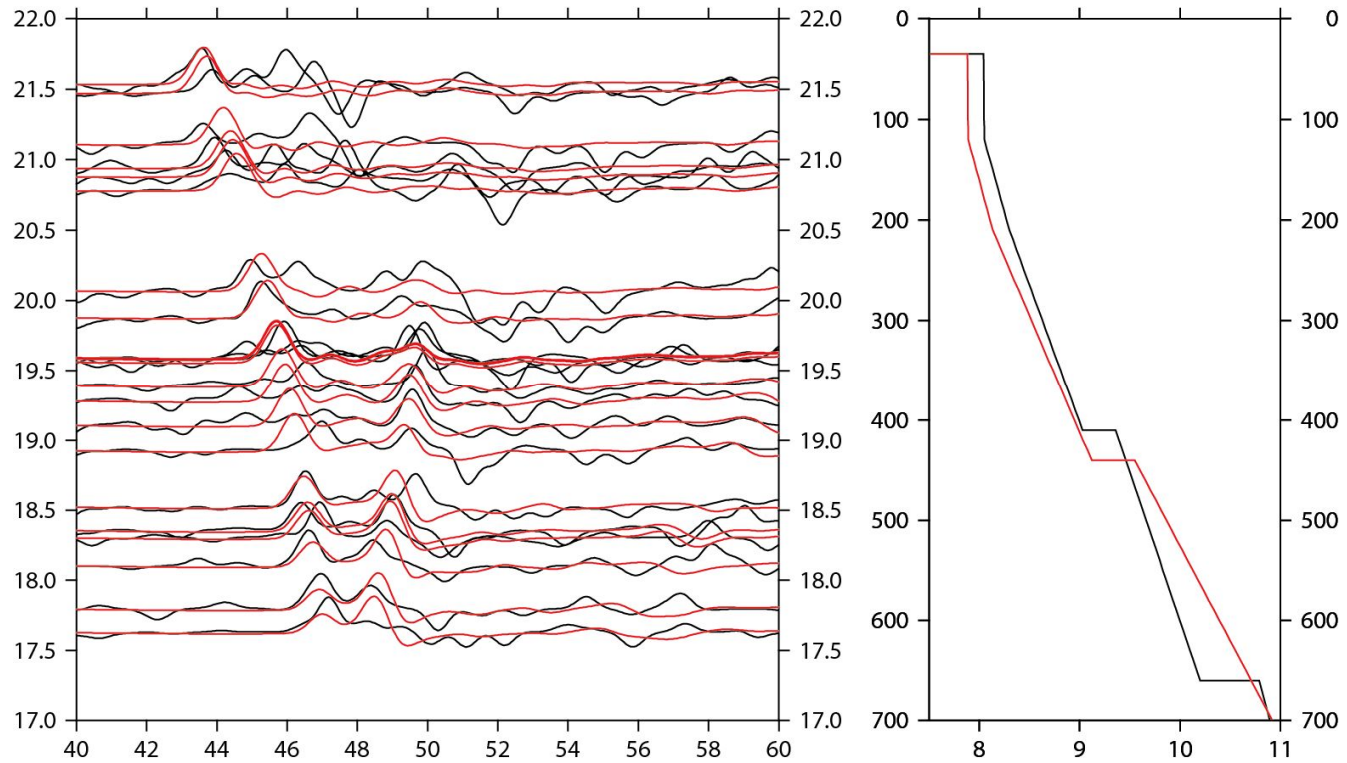


Figure 16 Best model after fitting for one linear structure between 410 and 660. The first arrivals near 19° does not fit well.

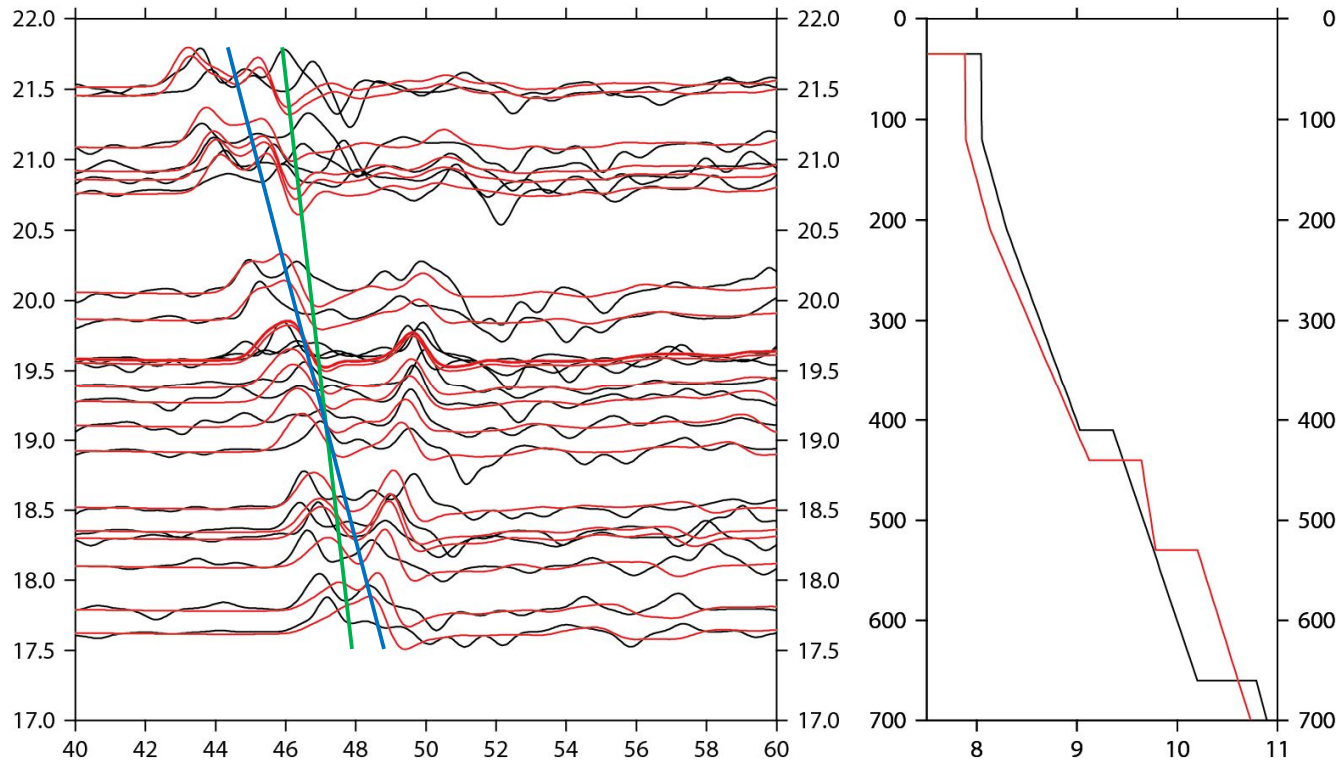


Figure 17 The best model. The phase between the 440 and 530 follows the green line and that below the 530 follows blue line.

Chapter 6. Discussion

I searched the 1D structure model for 2 earthquakes with waveform modelling. To find the best model, variance reduction of each event-model-station pairs is calculated. However, the variance reduction sometimes failed to find the best model. Most of those cases were due to matching the first arrivals of observations with the second or third phases of synthetics. In other cases, slowness of a phase is very different from the observations but the shifted waveforms match well. This is because the variance reduction only cares about the matching of the selected section. These errors could be removed by manual inspections easily, but if the data is large, other constraints such as arrival times will be needed to reduce them.

The small variance reduction of synthetic waveforms was another problem. During the synthetic tests, I supposed that waveforms are different when variance reduction is less than 80. However, even the model with maximum variance reduction could not exceed 70. Some models showed large variance reductions in specific stations, but averaging them lowered variance reductions. Noise, local anomalies, or unknown phases included in the waveform may be the cause of this low variance reduction.

The best model has low velocity in the upper mantle and its 410 discontinuity is deeper than IASP91 model. This is consistent to the previous studies with mantle tomography and receiver functions.

The 410 depth in northern Philippine Sea is known to be 432 ± 12 km [Seutsugu et al., 2010] and that of this study is 440 km. Slow velocity anomaly decreases as the depth increases to 410 and this also coincides with the previous study [Li and van der Hilst, 2010]. This slow upper mantle is explained to be hot mantle wedge.

The velocity structure is more complex beneath the 410 discontinuity. Slightly faster upper layer and the velocity jump at the 530 km depth in this result are similar to the M3.11 model [Tajima and Grand, 1995]. But the top of upper layer is fast and bottom is normal in this study while M3.11 has normal top and fast bottom. However, M3.11 can be used to explain the fast lower layer well since its velocity jump (maximum 2.5%) is similar to that of this study (3%). The best model could not catch the reduction of anomaly near the 660 km in M3.11 model, but the rays used in this study sample at most 570 km depth, so it is acceptable. The velocity jump at 525 km in M3.11 model is explained by the flattening and piling up of the slab. The sampling region of this study is also known to have stagnant slab [Seutsugu et al., 2010], so this result supports the previous studies.

Chapter 7. Conclusion and further studies

In this study, 410 triplicated waveforms observed in Korean seismic stations are modelled with Kennett reflectivity code. The final model has slow upper mantle, deeper 410 discontinuity, and fast transition zone with faster stagnant slab layer. This result matches well to the structures from previous studies such as hot, slow mantle wedge or fast stagnant slab.

Even though the result in this study seems good in this study, further work is required to this study. The arrival times in synthetics well matched to the observation, but the amplitude ratio between each phase does not match to the observation. Especially in the closest observations, the observation has much larger amplitude in first arrival while the synthetic has very small amplitude. Also, the broadening of waveforms between 19° to 19.5° range should be explained for better fitting.

More data is required to make better regional model. Those events excluded with 660 triplicated phases will help modelling the structure between the 410 and 660 discontinuities. There could be local anomalies affecting specific ray paths or stations, but small number of data and events made it hard to find them. Such anomalies may come from lateral changes of materials or 2D and 3D geometric changes of structure [Wang et al., 2014]. The subducting slab that cuts the ray path and lateral anomalies are hard to

consider in the Kennett reflectivity code since it uses 1D velocity structure. To figure out the effects of such structures, more data and better waveform modelling methods will be required.

References

- Cornwell, D. G., G. Hetényi, and T. D. Blanchard (2011), Mantle transition zone variations beneath the Ethiopian Rift and Afar: Chemical heterogeneity within a hot mantle?: ETHIOPIAN MANTLE TRANSITION ZONE VARIATIONS, *Geophys. Res. Lett.*, 38(16), n/a–n/a, doi:10.1029/2011GL047575.
- Day, E. A., and A. Deuss (2013), Reconciling PP and P'P' precursor observations of a complex 660 km seismic discontinuity, *Geophys. J. Int.*, 194(2), 834–838, doi:10.1093/gji/ggt122.
- Deuss, A. (2006), The Nature of the 660–Kilometer Discontinuity in Earth's Mantle from Global Seismic Observations of PP Precursors, *Science*, 311(5758), 198–201, doi:10.1126/science.1120020.
- Flanagan, M. P., and P. M. Shearer (1998), Topography on the 410–km seismic velocity discontinuity near subduction zones from stacking of sS, sP, and pP precursors, *J. Geophys. Res. Solid Earth*, 103(B9), 21165–21182, doi:10.1029/98JB00595.
- Fuchs, K., and G. Müller (1971), Computation of synthetic seismograms with the reflectivity method and comparison with observations, *Geophys. J. Int.*, 23(4), 417–433.
- Fukao, Y., M. Obayashi, and T. Nakakuki (2009), Stagnant Slab: A Review, *Annu. Rev. Earth Planet. Sci.*, 37(1), 19–46, doi:10.1146/annurev.earth.36.031207.124224.
- Gao, Y., D. Suetsugu, Y. Fukao, M. Obayashi, Y. Shi, and R. Liu (2010), Seismic discontinuities in the mantle transition zone and at the top of the lower mantle beneath eastern China and Korea: Influence of the stagnant Pacific slab, *Phys. Earth Planet. Inter.*, 183(1–2), 288–295, doi:10.1016/j.pepi.2010.03.009.
- Gudmundsson, Ó., and M. Sambridge (1998), A regionalized upper mantle (RUM) seismic model, *J. Geophys. Res. Solid Earth*, 103(B4), 7121–7136, doi:10.1029/97JB02488.
- Huang, J., and D. Zhao (2006), High–resolution mantle tomography of China and surrounding regions, *J. Geophys. Res.*, 111(B9),

doi:10.1029/2005JB004066.

- Inoue, T. (1994), Effect of water on melting phase relations and melt composition in the system $\text{Mg}_2\text{SiO}_4\text{--MgSiO}_3\text{--H}_2\text{O}$ up to 15GPa, *Phys. Earth Planet. Inter.*, 85(3–4), 237 – 263, doi:[http://dx.doi.org/10.1016/0031-9201\(94\)90116-3](http://dx.doi.org/10.1016/0031-9201(94)90116-3).
- Katsura, T., and E. Ito (1989), The system $\text{Mg}_2\text{SiO}_4\text{--Fe}_2\text{SiO}_4$ at high pressures and temperatures: Precise determination of stabilities of olivine, modified spinel, and spinel, *J. Geophys. Res. Solid Earth*, 94(B11), 15663–15670, doi:10.1029/JB094iB11p15663.
- Kennett, B. (1983), *Seismic Wave Propagation in Stratified Media*.
- Li, C., and R. D. van der Hilst (2010), Structure of the upper mantle and transition zone beneath Southeast Asia from traveltime tomography, *J. Geophys. Res.*, 115(B7), doi:10.1029/2009JB006882.
- Ligorria, J. P., and C. J. Ammon (1999), Iterative deconvolution and receiver–function estimation, *Bull. Seismol. Soc. Am.*, 89(5), 1395–1400.
- Li, J., X. Wang, X. Wang, and D. A. Yuen (2013), P and SH velocity structure in the upper mantle beneath Northeast China: Evidence for a stagnant slab in hydrous mantle transition zone, *Earth Planet. Sci. Lett.*, 367, 71–81, doi:10.1016/j.epsl.2013.02.026.
- Litasov, K. D., E. Ohtani, and A. Sano (2006), Influence of water on major phase transitions in the Earth’s mantle, *Earths Deep Water Cycle*, 95–111.
- Li, X., R. Kind, K. Priestley, S. V. Sobolev, F. Tilmann, X. Yuan, and M. Weber (2000), Mapping the Hawaiian plume conduit with converted seismic waves, *Nature*, 405(6789), 938–941, doi:10.1038/35016054.
- Obayashi, M., J. Yoshimitsu, and Y. Fukao (2009), Tearing of stagnant slab, *Science*, 324(5931), 1173–1175, doi:10.1126/science.1172496.
- Rickers, F., A. Fichtner, and J. Trampert (2013), The Iceland–Jan Mayen plume system and its impact on mantle dynamics in the

- North Atlantic region: Evidence from full-waveform inversion, *Earth Planet. Sci. Lett.*, 367, 39–51, doi:10.1016/j.epsl.2013.02.022.
- Saikia, C. K. (1994), Modified frequency-wavenumber algorithm for regional seismograms using Filon's quadrature: modelling of Lg waves in eastern North America, *Geophys. J. Int.*, 118(1), 142–158.
- Sambridge, M. (2002), Monte Carlo methods in geophysical inverse problems, *Rev. Geophys.*, 40(3), doi:10.1029/2000RG000089.
- Song, T.-R. A., D. V. Helmberger, and S. P. Grand (2004), Low-velocity zone atop the 410-km seismic discontinuity in the northwestern United States, *Nature*, 427(6974), 530–533.
- Suetsugu, D. et al. (2010), Depths of the 410-km and 660-km discontinuities in and around the stagnant slab beneath the Philippine Sea: Is water stored in the stagnant slab?, *Phys. Earth Planet. Inter.*, 183(1–2), 270–279, doi:10.1016/j.pepi.2010.09.004.
- Tajima, F., and S. P. Grand (1998), Variation of transition zone high-velocity anomalies and depression of 660 km discontinuity associated with subduction zones from the southern Kuriles to Izu-Bonin and Ryukyu, *J. Geophys. Res. Solid Earth*, 103(B7), 15015–15036, doi:10.1029/98JB00752.
- Tajima, F., I. Katayama, and T. Nakagawa (2009), Variable seismic structure near the 660km discontinuity associated with stagnant slabs and geochemical implications, *Phys. Earth Planet. Inter.*, 172(3–4), 183–198, doi:10.1016/j.pepi.2008.09.013.
- Takeuchi, N. et al. (2014), Upper mantle tomography in the northwestern Pacific region using triplicated P waves, *J. Geophys. Res. Solid Earth*, 119(10), 7667–7685, doi:10.1002/2014JB011161.
- Wang, T., J. Revenaugh, and X. Song (2014), Two-dimensional/three-dimensional waveform modeling of subducting slab and transition zone beneath Northeast Asia: 2D/3D WAVEFORM MODELING OF SLAB AND TZ, *J.*

- Geophys. Res. Solid Earth, 119(6), 4766–4786, doi:10.1002/2014JB011058.
- Weidner, D. J., and Y. Wang (1998), Chemical- and Clapeyron-induced buoyancy at the 660 km discontinuity, *J. Geophys. Res. Solid Earth*, 103(B4), 7431–7441, doi:10.1029/97JB03511.
- Wood, B. J. (1995), The Effect of H₂O on the 410-Kilometer Seismic Discontinuity, *Science*, 268(5207), 74–76, doi:10.1126/science.268.5207.74.
- Yusa, H., M. Akaogi, and E. Ito (1993), Calorimetric study of MgSiO₃ garnet and pyroxene: Heat capacities, transition enthalpies, and equilibrium phase relations in MgSiO₃ at high pressures and temperatures, *J. Geophys. Res. Solid Earth*, 98(B4), 6453–6460, doi:10.1029/92JB02862.
- Zhao, D. (2004), Global tomographic images of mantle plumes and subducting slabs: insight into deep Earth dynamics, *Phys. Earth Planet. Inter.*, 146(1–2), 3–34, doi:10.1016/j.pepi.2003.07.032.
- Zhu, H., E. Bozdağ, D. Peter, and J. Tromp (2012), Structure of the European upper mantle revealed by adjoint tomography, *Nat. Geosci.*, 5(7), 493–498, doi:10.1038/ngeo1501.
- Zhu, L., and L. A. Rivera (2002), A note on the dynamic and static displacements from a point source in multilayered media, *Geophys. J. Int.*, 148(3), 619–627.

Abstract

맨틀 전이대와 그 불연속면은 맨틀 대류와 그에 따라 발생하는 다양하고 복잡한 현상들을 연구하는데 있어 중요한 지역이다. 북서 태평양 지역은 많은 지진과 관측소가 있어 이러한 맨틀 내부 구조를 연구하기에 좋은 지역이다. 트리플리케이션은 지진파가 불연속면 근처를 지나면서 비슷한 위상이 여러 번 들어오는 것으로 불연속면 근처의 속도 구조에 대한 정보를 지닌다. 이 트리플리케이션이 기록된 지진파형을 모델링하면 맨틀 전이대 근처의 상세한 구조를 파악할 수 있다. 한반도의 지진관측소에서 관측된 이주-보닌-마리아나 해구의 두 지진의 합성 파형을 모델링하여 맨틀 불연속면 근처의 속도구조를 연구하였다. 각 지진에 대하여 모델을 그리드 서치법을 사용하여 합성 파형과 관측 파형의 오차를 계산해 비교하였으며 두 지진의 가장 잘 맞는 모델에서 비슷한, 느린 상부 맨틀과 깊은 410 불연속면의 구조가 나타났다. 두 지진을 동시에 맞추며 더 잘 설명할 수 있는 모델을 만들기 위하여 모델의 계산된 도달 시각과 실제 도달 시각을 비교한 후 합성 파형을 계산하였다. 이를 위해 불연속면 위를 지나오는 파형의 도달 시각을 맞추는 모델을 먼저 찾은 다음 보다 깊은 곳을 지나오는 파형의 도달시각을 맞췄다. 가장 잘 맞는 모델에서 상부맨틀은 2% 느리고 410 불연속면은 440km에 위치하며 530km 아래로 3% 빠른 층이 존재한다. 이러한 모델은 이전 연구에서 밝혀진 필리핀 해 아래의 맨틀 웨지와 정체된 슬랩과 일치한다.

주요어 : 맨틀 전이대, 북서 태평양, 필리핀 해 북부, 트리플리케이션, 정체된 슬랩, 맨틀 웨지, 파형 모델링